Dependence of calcium phosphate formation on nanostructure of rutile TiO2(110) surfaces

Sasahara, Akira
Murakami, Tatsuya
Tomitori, Masahiko

(Citation)
Japanese Journal of Applied Physics,57(11):115501-115501

(Issue Date)
2018-11

(Resource Type)
journal article

(Version)
Accepted Manuscript

(URL)
https://hdl.handle.net/20.500.14094/90005261

Dependence of calcium phosphate formation on nanostructure of rutile TiO_2(110) surfaces

Akira Sasahara[1*], Tatsuya Murakami[2], and Masahiko Tomitori[2]

[1] *Kobe University, Kobe 657-8501, Japan*

[2] *Japan Advanced Institute of Science and Technology, Nomi, Ishikawa 923-1292, Japan*

[*] E-mail: sasahara@harbor.kobe-u.ac.jp

To demonstrate the effect of the surface nanostructures on the osteoconductivity of titanium dioxide (TiO_2), formation of calcium phosphate on the rutile TiO_2(110) surfaces in Hanks' balanced salt solution (HBSS) was examined using X-ray photoelectron spectroscopy (XPS) and atomic force microscopy (AFM) techniques. When the TiO_2(110) surfaces annealed in air were immersed in HBSS, calcium phosphate particles were formed on the surface. The calcium phosphate formation was suppressed by further annealing of the surfaces in O_2 before the immersion in HBSS. The suppression of calcium phosphate formation is attributed to the transformation of the topmost layer of the air-annealed TiO_2(110) surface from amorphous to rutile. The arrangement of the phosphate ions adsorbed on the rutile (1×1) surface does not match the hydrogen phosphate ion lattice of the $CaHPO_4$ sheet of brushite.

1. Introduction

Titanium and its alloys have been accepted to be suitable for biomedical implants1). Besides their nontoxicity, high corrosion resistance, and bonelike mechanical properties, their osteoconductivity underlies their biocompatibility. When Ti implants are embedded in the living body, calcium phosphate is formed on their surface and transforms into hydroxyapatite [$Ca_{10}(PO_4)_6(OH)_2$], which is the main component of bones2-4). The Ti implants bond to living bones through the hydroxyapatite layer. The osteoconductivity of the implants needs to be promoted for replacement implants such as artificial knees and hip joints that have to be quickly and tightly fixed to the host bones5,6). On the other hand, suppression of osteoconductivity is favorable for the safe removal of bone fixators from the broken bones after they are rejoined5,7). Thus, controlling osteoconductivity is an essential requirement for Ti implants. Calcium phosphate formation at the initial stage of the implant-bone bonding process is the key to controlling osteoconductivity.

The osteoconductivity of Ti implants arises from the natural oxide film covering them. Hanawa and Ota examined the surface composition of Ti plates immersed in a simulated body fluid by an X-ray photoelectron spectroscopy (XPS) technique8). On the basis of depthwise analysis, calcium phosphate was concluded to be formed on titanium dioxide (TiO_2) covering the Ti plate. Chusuei et al. applied secondary-ion mass spectroscopy technique to the characterization of calcium phosphate formed on the TiO_2 film in aqueous solutions containing $CaCl_2$ and $KH_2PO_4$9). From the ratios of PO_3^- to PO_2^- ions reflecting the composition of calcium phosphate, they concluded that dicalcium phosphate dihydrate [$CaHPO_4{\cdot}2H_2O$], which is referred to as brushite, is the predominant form of calcium phosphate. Kokubo et al. found that alkaline treatment and subsequent annealing induced the activity of TiO_2 covering Ti for apatite formation10). On the basis of structural, compositional, and surface potential analyses, they proposed that alkaline treatment induced $Na_2Ti_5O_{11}$ formation on the topmost layer of TiO_2. Calcium phosphate formation was explained to be initiated by the bonding of calcium ions to the OH groups terminating the $Na_2Ti_5O_{11}$ surface layer. They also found that acid treatment, instead of alkaline treatment, formed a positively charged TiO_2 layer on Ti metal11). On such a TiO_2 layer, adsorption of phosphate ions (PO_4^{3-}) was promoted.

TiO_2 has three natural crystal phases, namely, anatase, brookite, and rutile, which are differentiated from their TiO_6 octahedral arrangement. Among the three phases, comparative osteoconductivity tests have been performed for anatase and rutile. Uchida et al. prepared amorphous, anatase, and rutile TiO_2 films by the sol-gel method and examined apatite formation thereon by immersing the films in simulated body fluid[12]. Anatase TiO_2 was found to have the highest activity for the apatite formation. Assuming the epitaxial growth of apatite, the high osteoconductivity of anatase was explained by the good lattice matching between the (110) surface of anatase TiO_2 and the (0001) surface of apatite. Rohanizadeh et al. coated Ti discs with microparticles of anatase or rutile TiO_2 from their slurries and immersed the discs in a calcium phosphate solution[13]. The higher yield of apatite on anatase TiO_2 than on rutile TiO_2 was attributed to the higher density of OH groups on the former. The OH groups act as the nucleation sites for apatite. Yamamoto et al. found that heating in air decreased the bone-implant contact ratio of anatase TiO_2 film to the same extent as that of rutile TiO_2 film[14]. On the basis of water-wettability analysis, they concluded that osteoconductivity was dependent on the density of surface OH groups and independent of the crystal phase. The results of these studies showed that apatite formation is sensitive to the nanostructures of the TiO_2 surface such as atom arrangement and OH groups.

Single-crystal surfaces are useful for examining the effects of surface nanostructures because of their structural and compositional uniformity. Rutile TiO_2 surfaces have been widely studied as models of TiO_2-based products such as catalysts and electrodes, because large size and high-quality crystals are commercially available[15]. Murphy et al. reported the calcium phosphate formation on the rutile $TiO_2(110)$ surface in aqueous solutions of $CaCl_2$ and KH_2PO_4[16)]. By using the $TiO_2(110)$ surface with a well-defined structure obtained by aqua regia and UV-ozone treatments, they found that the induction period of calcium phosphate formation on the $TiO_2(110)$ surface was equivalent to that on the $Al_2O_3(0001)$ surface. They proposed that the kinetics of calcium phosphate formation was dependent on the morphology of the substrate surfaces rather than their chemical natures.

In the present study, the dependence of calcium phosphate formation on the surface nanostructure was examined on rutile $TiO_2(110)$ surfaces annealed in air. **Figure 1** shows the simple truncation of the bulk rutile TiO_2 at the (110) plane. Oxygen atoms that coordinated to two Ti atoms, which are hereafter referred to as bridging O atoms (O_b), are aligned along the [001] direction to form protruding rows. Ti atoms that coordinated to five O atoms (Ti_{5c}) are exposed at the trenches between the O_b atom rows and are aligned to form rows along the [001] direction. This (1×1) surface is prepared by sputter-anneal cleaning in ultrahigh vacuum (UHV). Unlike the cleaning in UHV, annealing in air makes the topmost layer of the $TiO_2(110)$ surface amorphous[17)]. Recently, it has been found that the amorphous topmost layer of the air-annealed surface transforms to a rutile (1×1) structure after annealing in O_2 at atmospheric pressure[17]. The TiO_2(110) surfaces prepared in ambient pressure environments are demonstrated to have different properties for calcium phosphate formation.

2. Experimental methods

Mirror-polished rutile TiO_2(110) wafers (Shinkosha) were ultrasonically degreased in acetone, etched in a 10% hydrofluoric acid, and ultrasonically washed in Milli-Q water. Then, the wafers were smoothened by annealing at 1273 K for 12 h in a sapphire tube placed in a tube furnace. Subsequent annealing in O_2 was carried out in a quartz tube at 773 K for 1 h. The pressure and flow rate of O_2 were controlled by a gas regulator to 1.3×10^5 Pa and 0.5 L/min, respectively. Under this O_2 annealing condition, no Si evaporation from the quartz tube[18,19] occurred.

The formation of calcium phosphate was tested by immersing the TiO_2 wafers in 100 mL of HBSS (with Ca and Mg and without phenol red, Nacalai Tesque) at room temperature. HBSS is a type of simulated body fluid reproducing ion concentrations of human blood plasma[20]. The perfluoroalkoxy alkane container for HBSS was shaded during the test. During the 4 week immersion, HBSS was replaced with a fresh one every 1 week. The pH of the fresh HBSS was ~7.0 and increased to ~7.9 after 1 week of incubation in the container, regardless of the presence or absence of the TiO_2 wafer. After the immersion, the wafers were rinsed in Milli-Q water for 1 min to remove physically adsorbed ions.

XPS analysis was performed using a commercial instrument (Kratos Axis Ultra DLD) with a base pressure of 6×10^{-7} Pa. The monochromatic Al Kα line was used as an excitation source, and charging of the samples was minimized by using a low-energy electron neutralizer. The photoelectron emission angle with respect to the surface normal was set to 0°. The pass energy of the analyzer and the energy step were 160 and 1.0 eV for survey scans and 20 and 0.1 eV for fine scans, respectively. The binding energy of spectra was calibrated such that the Ti $2p_{3/2}$ peak from the bulk TiO_2 was 459.1 eV. With this calibration, the O 1s peak from the O atoms of the bulk TiO_2 (O_{bulk} atoms) was corrected to 530.3 eV. The spectra were fitted using Gaussian−Lorentzian curves (70:30) after Shirley-type background subtraction.

Contact-mode atomic force microscopy (AFM) imaging was performed using a commercial microscope (Agilent Technologies SPM 5500) in air. Silicon nitride cantilevers with a nominal spring constant of 0.6 N/m (OLYMPUS OMCL-TR800PSA-1) were used as a probe. Images are presented without filtering, and the root mean square surface roughness were measured after smoothing with a 9-point median filter.

3. Results and discussion

Figure 2 shows the survey scan XPS spectra of the $TiO_2(110)$ surfaces annealed in air. The intense peaks at ~460 and ~530 eV are from Ti 2p and O 1s photoelectrons, respectively. Spectrum a of the as-prepared surface shows that the impurity elements were C and Na. Carbon originated from organic adsorbates from laboratory air. Na giving the faint peak overlapping the Ti LMM Auger peak is an intrinsic impurity of the wafer. Spectrum b was obtained for the surface immersed in HBSS for 1 h. Ca and P peaks appeared, and other elements included in HBSS such as Cl, Mg, S, and K, were under the detection limit. The nondeposition of other elements except for Ca and P has been found in a previous study on TiO_2 nanocrystalline films8). Na on the as-prepared surface would have been in an oxide form and dissolved into HBSS. The Ca and P peaks were greatly enhanced after 1 week immersion, as shown in spectrum c. The Ti peaks were reduced to an unrecognizable level. Mg peaks, which were not detected after the 1 h immersion, emerged.

The chemical states of the elements found by the survey scan were examined by the fine scan of their primary regions. **Figure 3** shows the sets of the fine scan XPS spectra of the surfaces shown in **Fig. 2**. Panel a shows the spectra of the as-prepared surface. The major O 1s peak at 530.3 eV originates from O_{bulk} atoms. The high-binding-energy shoulder of the O_{bulk} peak originates from the OH groups and O_b atoms21). The Ti $2p_{3/2}$ peak was free from the low-binding-energy shoulder at ~457.0 eV that originates from Ti cations with lower-valence states, Ti^{n+} ($n<4$)22,23). This indicates that the Ti atoms were fully oxidized. The C 1s spectrum was fitted by three peaks at 285.7, 287.1, and 289.1 eV that are assigned to C atoms involved in C–C/C–H, C–O, and O–C=O bonds ($C_{C-C/C-H}$, C_{C-O}, and $C_{O-C=O}$ atoms), respectively24). These are typical features of the O 1s, Ti 2p, and C 1s spectra of TiO_2 surfaces annealed in air17). No specific structure was observed in the Ca 2p and P 2p regions. The hump with a peak at ~51.5 eV in the Mg 2p region is a shake-up satellite of the Ti 3p peak25).

Panel b shows the spectra of the surface immersed in HBSS for 1 h. The O_{bulk} peak showed little change in its binding energy and full width at half maximum (FWHM). The shoulder of the O_{bulk} peak was slightly elevated at 531.7 and 533.5 eV. The Ti $2p_{3/2}$ peak as well as the O_{bulk} peak appeared identical to those of the as-prepared surface shown in panel a. Ca $2p_{3/2}$ and Ca $2p_{1/2}$ peaks emerged at 347.8 and 351.4 eV, respectively, in the

Ca 2p region. A single asymmetric peak was observed in the P 2p region at 133.7 eV. The peak was fitted by two peaks at 133.6 and 134.5 eV with an intensity ratio of 2:1. The two peaks were assigned to the P $2p_{3/2}$ and P $2p_{1/2}$ peaks. The relative intensity of the C_{C-O} peak to the C_{C-H} peak increased to 0.77, which was 5.5 times as high as that on the air-annealed surface of 0.14. The peak of the hump in the Mg 2p region slightly shifted to the lower binding energy side, but the shift was not distinct.

The Ca $2p_{3/2}$ peak was separated from the Ti $2p_{3/2}$ peak by 111.3 eV. The binding energy separation indicates that Ca atoms are in a divalent cation form26). The P 2p peak was separated from the Ti $2p_{3/2}$ peak by 325.4 eV, which indicates that P atoms are in phosphate form26). That the peak was fitted with a single pair of spin-orbit split peaks indicates that the P atoms were present on the air-annealed surfaces in an identical chemical state. The elevation at 531.7 and 533.5 eV in the O 1s region spectra is attributed to the adsorption of phosphate ions27). The phosphate ions are coordinated to Ti atoms exposed on the air-annealed surface28). The coordination of the phosphate ions did not reduce the surface Ti atoms, as indicated by the absence of the low-binding-energy shoulder of the Ti $2p_{3/2}$ peak. Such independence of the chemical state of the surface Ti atoms from adsorbates has been found for phosphate ions 27) as well as trimethyl acetic acid29), methanol30), and malonic acid molecules31).

The intensity ratio of the Ca 2p peak to the P 2p peak was 3.3. By using the factory-provided relative sensitivity factors of 1.833 for Ca 2p and 0.486 for P 2p of photoelectrons, we calculated the Ca/P atom ratio to be 0.9. The Ca/P atom ratio of 0.9 is close to that of dicalcium phosphate in either dehydrate form (brushite) or anhydrate form (monetite) among the biologically relevant calcium phosphates32). The brushite, which has been reported as a precursor of the hydroxyapatite, is a more likely candidate for calcium phosphate formed on the TiO_2(110) surface9,33,34). The increase in C_{C-O} peak intensity relative to the $C_{C-C/C-H}$ peak intensity is attributed to the adsorption of glucose27). Glucose is coordinated to the surface of TiO_2 nanoparticles in monodentate or bridging form via the Ti-O bond35). Glucose may have higher affinity to brushite than to the TiO_2 surface.

Panel c shows the spectra of the surface immersed in HBSS for 1 week. The O 1s region spectrum was fitted by two peaks at 531.7 and 533.4 eV. The Ti $2p_{3/2}$ peak was reduced to barely detectable to be used for binding energy calibration. The Ca 2p and P 2p peaks became intense with no binding energy shift. Although comparison of the absolute peak intensity is not possible, the C 1s peaks appeared to be stronger than those in panels a and b. The relative intensity of the C_{C-O} peak with respect to the $C_{C-C/C-H}$ peak was 0.24 and was reduced to 1/3 of that of the surface immersed for 1 h. A distinct peak at 51.1 eV appeared in the Mg 2p region.

The growth of the two O 1s peaks at 531.7 and 533.4 eV and the disappearance of the O_{bulk} peak indicate that calcium phosphate was accumulated on the surface up to 2–3 nm thickness. The major O 1s peak at 531.7 eV had the FWHM of 1.3 eV, which was larger than that of the O_{bulk} peak, 1.0 eV. This reflects the presence of O atoms with chemically different states in the phosphate species, such as those bridging P and H atoms, terminating P atoms, and bridging P and surface Ti atoms. The great reduction in the intensity of the Ti $2p_{3/2}$ peak is also explained by the covering of the surface with calcium phosphate. The peak at 533.4 eV is mainly from H_2O molecules. H_2O molecules adsorbed on the TiO_2 surface give rise to the O 1s peak at binding energies higher than the O_{bulk} peak by 2.4–3.5 eV[36)]. The FWHMs of the Ca $2p_{3/2}$ and P $2p_{3/2}$ peaks were 1.4 and 1.3 eV, respectively. The FWHM and the binding energies of the Ca 2p and P 2p peaks were the same as those on the surface immersed for 1 h. The Ca and P atoms were in divalent and phosphate ions, respectively, to form calcium phosphate.

The intensity ratio of the Ca 2p peak to the P 2p peak was 4.5, and the Ca/P atom ratio was estimated to be 1.2 using the factory-provided relative sensitivity factors. Among the biologically relevant calcium phosphates, the octacalcium phosphate [$Ca_8(HPO_4)_2(PO_4)_4 \cdot 5H_2O$] has the Ca/P atom ratio closest to 1.2. As with brushite, the octacalcium phosphate is one of the possible calcium phosphates intermediate to hydroxyapatite. The transformation of brushite to octacalcium phosphate in a mixed aqueous solution of $Ca(NO_3)_2$ and KH_2PO_4 has been reported by Perez et al.[37)]. Octacalcium phosphates synthesized by various methods showed the Ca/P atom ratios of 1.23–1.33[38)]. The smaller Ca/P atom ratio of calcium phosphate on the $TiO_2(110)$ surface is explained by assuming that brushite as well as octacalcium phosphate were present on the surface. The brushite might have remained at the contact interface between the calcium phosphate layer and the $TiO_2(110)$ surface. Adsorption of Mg onto the octacalcium phosphate agrees with the previous report by Tung et al.[39)]. The distinct growth of the $C_{C\text{-}C/C\text{-}H}$ peak and the decrease in $C_{C\text{-}O}/C_{C\text{-}C/C\text{-}H}$ peak intensity ratio reflect the increase in the amount of organic contaminants during long-time immersion.

Precipitation of calcium phosphates was also observed by AFM. The air-annealed surface showed a step-terrace structure as shown in **Fig. 4(a)**. The step directions and the step-to-step distances were different from wafer to wafer, which reflects miscuts of the surfaces. An irregular morphology with a height fluctuation up to 0.16 nm was resolved on the terraces as shown in the inset. The roughness of the terraces was 0.3 nm. These features are the same as those observed by noncontact AFM operated in UHV[17]. **Figure 4(b)** shows the surface immersed in HBSS for 1 h. Particles with heights of 0.2–0.3 nm and diameters of 20–40 nm were uniformly distributed on the entire surface. Owing to the emergence of these particles, the roughness increased to 0.6 nm. The particles are assigned to brushite on the basis of XPS results. After 1 week immersion, the surface was covered by particles with diameters of 20–50 nm as shown in **Fig. 4(c)**. The covering of the surface with the particles is consistent with the disappearance of O_{bulk} and the Ti 2p peaks. The particles did not appear on the surface immersed in Milli-Q water for 1 week as shown in **Fig. 4(d)**. Therefore, the particles are not related to surface dissolution or deposition of contaminants.

The formation of calcium phosphates on the air-annealed surface contrasts with the (1×1) surface prepared in UHV. Calcium phosphate was not formed on the (1×1) surface even after 1 week immersion in HBSS[27]. The scanning tunneling microscopy images revealed that phosphate ions were packed to form a monolayer with a (2×1) periodicity with respect to the (1×1) structure. The (2×1) arrangement of the phosphate ions does not match the arrangement of the hydrogen phosphate ions in the $CaHPO_4$ sheet of brushite. The least lattice mismatch with the hydrogen phosphate ions in the $CaHPO_4$ sheet is achieved when the phosphate ions are arranged with c(2×2) periodicity on the (1×1) surface. However, the lattice mismatch is not less than 16%. Therefore, brushite is not formed on the (1×1) surface. On the other hand, the air-annealed surface has the topmost layer with an amorphous form[17]. The irregular arrangement of Ti atoms exposed on the amorphous layer could provide surface Ti atoms where phosphate ions can be arranged to be suitable for formation of the $CaHPO_4$ sheet.

Here, we consider the possible site for calcium phosphate formation on the air-annealed TiO_2 surface. The monatomic steps on the TiO_2 surface indicate that the second and lower layers were crystallized into the rutile structure. It is possible that a part of the amorphous topmost layer has the (1×1)-like local structure by reflecting the rutile structure of the second layer. Panel (i) of **Fig. 5(a)** shows the structure in which TiO_2 units including the bridging O atoms are removed from the topmost layer of the (1×1) surface shown in **Fig. 1**. The asterisk indicates the trench resulting from the removal of the TiO_2 units. Hydrogen phosphate ions are bound to two fivefold-coordinated Ti atoms in the bridging form via two O–Ti bonds[28]. The hydrogen phosphate ions are aligned along the [001] direction at intervals of 0.60 nm as shown in panel (ii) of **Fig. 5(b)**. The distance of 0.60 nm matches the distance between the hydrogen phosphate ions in the $CaHPO_4$ sheet of brushite along the *a*-axis shown in **Fig. 5(b)**. Assume that the phosphate ions adsorbed on the Ti atom rows are alternately out-of-phase along the $[1\bar{1}0]$ direction as shown in panel (ii) of **Fig. 5(a)**. The phosphate ions facing across the trenches could be inclined toward each other. When the distance between the phosphate ions across the trench is reduced to 0.62 nm, the distance between them matches the distance between the hydrogen phosphate ions in the $CaHPO_4$ sheet along the *c*-axis. Thus, brushite is likely to be formed on the basis of the adsorbed phosphate ions. Such $[1\bar{1}0]$-directed inclination of the phosphate ions is less possible for the c(2×2) arrangement on the (1×1) surface owing to the steric hindrance of bridging O atoms as shown in panel (iii) of **Fig. 5(a)**. Ca ions are not coordinated to the hydrogen phosphate ions separated from each other.

The calcium phosphate formation was examined on the air-annealed surfaces that was further annealed in O_2. **Figure 6** shows the survey scan XPS spectra of the O_2-annealed surfaces. Spectrum a obtained from the O_2-annealed surface was almost identical to that from the air-annealed surface, where only the peaks of Ti and O except for C and Na were observed. Unlike in the case of the air-annealed surface, no Ca and P peaks were observed after the immersion in HBSS for 1 h and 1 week as shown in spectra b and c, respectively. Even after the immersion was extended to 4 weeks, no Ca peaks were observed as shown in spectrum d. P peaks were very faint.

Figure 7 shows the sets of the fine scan XPS spectra of the O_2-annealed surfaces. Spectrum a of the O_2-annealed surface showed similar features to those of the air-annealed surface. The O 1s spectrum consisted of the intense O_{bulk} peak with the high-binding-energy shoulder. The Ti $2p_{3/2}$ peak showed no low-binding-energy shoulder. No features were observed in the Ca 2p, P 2p, and Mg 2p regions. Thus, the O_2-annealed surface is chemically identical to the air-annealed surface. Spectra b, c, and d were obtained from the O_2-annealed surfaces immersed in HBSS for 1 h, 1 week, and 4 weeks, respectively. Faint Ca $2p_{3/2}$, Ca $2p_{1/2}$, and P 2p peaks were observed and were obviously weaker than those of the air-annealed surface.

The suppression of calcium phosphate formation was also shown by AFM. **Figure 8(a)** shows an AFM topography image of the as-prepared surface before immersion in HBSS. No distinct difference from the air-annealed surface shown in **Fig. 8(a)** was found. **Figures 8(b)–8(d)** show the O_2-annealed surfaces immersed in HBSS for 1 h, 1 week, and 4 weeks, respectively. Unlike the air-annealed surfaces shown in **Figs. 4(b) and 4(c)**, calcium phosphate particles did not appear after 1 h immersion. Even after immersion for 4 weeks, no calcium phosphate particles were observed, and the step-terrace structure was clearly observed.

A possible interpretation of the suppression of calcium phosphate formation is the failure of epitaxial growth of brushite. Annealing in O_2 induces the transformation of the topmost layer from the amorphous phase to the rutile phase, which makes the surface have the (1×1) structure. As discussed above, the phosphate ions are not arranged on the (1×1) surface similarly to the hydrogen phosphate ions in the $CaHPO_4$ sheet of the brushite crystal. The lattice matching with brushite explains the osteoconductivity of the anatase $TiO_2$14). The amorphous layer covering the anatase TiO_2 surface is essentially equivalent to that covering the rutile TiO_2 surface. The smoothing of the amorphous layer by heating makes the osteoconductivities of the anatase and rutile TiO_2 surfaces comparable.

The structural change of the (1×1) surface may affect the density of the basic surface OH groups, which can be replaced by the hydrogen phosphate ions40). Fitts et al. obtained a pH of 4.8 for the point of zero charge of the air-annealed (110) surface using the sum-frequency-generation technique41). Hence, the air-annealed surface in HBSS with pHs of 7–8 is expected to be rich in OH groups. The O_2-annealed surface with the (1×1) structure may have less OH groups than the air-annealed surface. Wang et al. reported that the barrier height of H_2O molecule dissociation on the (1×1) surface is 0.36 eV and that H_2O molecules are energetically more stable than the OH groups with a barrier height of 0.035 eV42). The dissociation of H_2O molecules on the O_2-annealed surface may be limited. Actually, Serrano et al. assigned the spots in the STM image of the (1×1) surface obtained in pure water to H_2O molecules forming a hydrogen bonding network43). Thus, the lower density of OH groups on the O_2-annealed surface may appear to explain the suppression of calcium phosphate formation on it. However, phosphate ions can be adsorbed on the (1×1) surface along Ti_{5c} atom rows regardless of the OH groups27). Therefore, we could reasonably conclude that the structural change is responsible for the suppression of calcium phosphate formation.

4. Conclusions

Structure-sensitive calcium phosphate formation was demonstrated using a TiO_2 surface with unequivocally well-defined nanostructures. Calcium phosphate formation on the TiO_2(110) surface annealed in air was suppressed when the surface was further annealed in O_2 before immersion in HBSS. Annealing in O_2 induces transformation of the topmost layer from an amorphous structure to a rutile structure. The suppression of calcium phosphate formation on the O_2-annealed surface was explained by a failure of epitaxial growth of brushite due to the lattice mismatch. Phosphate ions adsorbed on the rutile (1×1) surface is not appropriate for Ca ions to be coordinated to form the $CaHSO_4$ layer of brushite.

Acknowledgments

This work was supported by Grants-in-Aid for Scientific Research from the Japan Society for the Promotion of Science (JSPS) KAKENHI Grant Numbers 24246014, 26600024, and 26630330.

References

1) D. M. Brunette, P. Tengvall, and P. Thomsen, in *Titanium in Medicine* (Springer, Berlin, 2001) 1st ed., Part IV, p. 457.

2) O. Borkiewicz, J. Rakovan, and C. L. Cahill, Am. Mineral. **95**, 1224 (2010).

3) A. Bannerman, R. L. Williams, S. C. Cox, and L. M. Grover, Sci. Rep. **6**, 1 (2016).

4) J. H. Shepherd, D. V. Shepherd, and S. M. Best, J. Mater. Sci.: Mater. Med. **23**, 2335 (2012).

5) T. Hanawa, Sci. Technol. Adv. Mater. **13**, 064102 (2012).

6) L. Le Guéhennec, A. Soueidan, P. Layrolle, and Y. Amouriq, Dent. Mater. **23**, 844 (2007).

7) F. M. Kovar, E. Strasser, M. Jaindl, G. Endler, and G. Oberleitner, Orthop. Traumatol. Surg. Res. **101**, 785 (2015).

8) T. Hanawa and M. Ota, Appl. Surf. Sci. **55**, 269 (1992).

9) C. C. Chusuei, D. W. Goodman, M. J. Van Stipdonk, D. R. Justes, K. H. Loh, and E. A. Schweikert, Langmuir **15**, 7355 (1999).

10) T. Kokubo, H. Kim, M. Kawashita, and T. Nakamura, J. Mater. Sci.: Mater. Med. **15**, 99 (2004).

11) T. Kokubo, D. K. Pattanayak, S. Yamaguchi, H. Takadama, T. Matsushita, T. Kawai, M. Takemoto, S. Fujibayashi, and T. Nakamura, J. R. Soc. Interface **7**, S503 (2010).

12) M. Uchida, H. Kim, T. Kokubo, S. Fujibayashi, and T. Nakamura, J. Biomed. Mater. Res. A **64**, 164 (2003).

13) R. Rohanizadeh, M. Al-Sadeq, and R. Z. LeGeros, J. Biomed. Mater. Res. A **71**, 343 (2004).

14) D. Yamamoto, I. Kawai, K. Kuroda, R. Ichino, M. Okido, and A. Seki, Bioinorg. Chem. and Appl. **2012**, 495218 (2012).

15) U. Diebold, Surf. Sci. Rep. **48**, 53 (2003).

16) M. Murphy, M. S. Walczak, H. Hussain, M. J. Acres, C. A. Muryn, A. G. Thomas, N. Silikas, and R. Lindsay, Surf. Sci. **646**, 146 (2016).

17) A. Sasahara, T. Murakami, L. T. U. Tu, and M. Tomitori, Appl. Surf. Sci. **428**, 1000 (2018).

18) T. T. U. Le, A. Sasahara, and M. Tomitori, J. Phys. Chem. C **117**, 23621 (2013).

19) A. Sasahara, C. L. Pang, and M. Tomitori, J. Phys. Chem. C **114**, 20189 (2010).

20) J. H. Hanks and R. E. Wallace, Proc. Soc. Exp. Biol. Med. **71**, 196 (1949).

21) A. Sasahara and M. Tomitori, J. Phys. Chem. C **120**, 21427 (2016).

22) A. Sasahara and M. Tomitori, J. Phys. Chem. C **117**, 17680 (2013).

23) W. Göpel, J. A. Anderson, D. Frankel, M. Jaehnig, K. Phillips, J. A. Schäfer, and G. Rocker, Surf. Sci. **139**, 333 (1984).

24) E. McCafferty and J. P. Wightman, Surf. Interface Anal. **26**, 549 (1998).

25) K. S. Kim and N. Winograd, Chem. Phys. Lett. **31**, 312 (1975).

26) T. Hanawa and M. Ota, Biomaterials **12**, 767 (1991).

27) A. Sasahara, T. Murakami, and M. Tomitori, Surf. Sci. **668**, 61 (2018).

28) P. A. Connor and A. J. McQuillan, Langmuir **15**, 2916 (1999).

29) J. M. White, J. Szanyi, and M. A. Henderson, J. Phys. Chem. B **108**, 3592 (2004).

30) P. M. Jayaweera, E. L. Quah, and H. Idriss, J. Phys. Chem. C **111**, 1764 (2007).

31) K. L. Syres, A. G. Thomas, D. M. Graham, B. F. Spencer, W. R. Flavell, M. J. Jackman, and V. R. Dhanak, Surf. Sci. **626**, 14 (2014).

32) S. V. Dorozhkin and M. Epple, Angew. Chem., Int. Ed. **41**, 3130 (2002).

33) R. E. Wuthier, G. S. Rice, J. E. B. Wallace, Jr., R. L. Weaver, R. Z. LeGeros, and E. D. Eanes, Calcif. Tissue Int. **37**, 401 (1985).

34) S. Ucara, S. H. Bjørnøy, D. C. Bassett, B. L. Strand, P. Sikorski, and J. Andreassen, J. Cryst. Growth **468**, 774 (2017).

35) G. Kim, S. Lee, and W. Choi, Appl. Catal. B **162**, 463 (2015).

36) G. Ketteler, S. Yamamoto, H. Bluhm, K. Andersson, D. E. Starr, D. F. Ogletree, H. Ogasawara, A. Nilsson, and M. Salmeron, J. Phys. Chem. C **111**, 8278 (2007).

37) L. Perez, L. J. Shyu, and G. H. Nancollas, Colloids Surf. **38**, 295 (1989).

38) O. Suzuki, Acta Biomater. **6**, 3379 (2010).

39) M. S. Tung, B. Tomazic, and W. E. Brown, Arch. Oral Biol. **37**, 585 (1992).

40) K. E. Healy and P. Ducheyne, Biomaterials **13**, 553 (1992).

41) J. P. Fitts, M. L. Machesky, D. J. Wesolowski, X. Shang, J. D. Kubicki, G. W. Flynn, T. F. Heinz, and K. B. Eisenthal, Chem. Phys. Lett. **411**, 399 (2005).

42) Z. Wang, Y. Wang, R. Mu, Y. Yoon, A. Dahal, G. K. Schenter, V. Glezakou, R. Rousseau, I. Lyubinetsky, and Z. Dohnalek, Proc. Natl. Acad. Sci. U. S. A. **114**, 1801 (2017).

43) G. Serrano, B. Bonanni, M. Giovannantonio, T. Kosmala, M. Schmid, U. Diebold, A. Carlo, J. Cheng, J. VandeVondele, K. Wandelt, and C. Goletti, Adv. Mater. Interfaces **2**, 1500246 (2015).

Figure Captions

Figure 1. (Color online) Ball-and-stick model of the rutile $TiO_2(110)$-(1×1) surface. Small light blue balls and large red balls represent Ti and O atoms, respectively.

Figure 2. Survey scan XPS spectra of the air-annealed $TiO_2(110)$ surfaces. (a) As-prepared surface. (b,c) Surfaces immersed in HBSS for (b) 1 h and (c) 1 week.

Figure 3. Sets of O 1s, Ti $2p_{3/2}$, Ca 2p, C 1s, P 2p, and Mg 2p XPS spectra of the air-annealed $TiO_2(110)$ surfaces. The fitting peaks of P 2p spectra in (b, c) and Ti $2p_{3/2}$ spectrum in (c) are represented by thin black line. (a) As-prepared surface. (b, c) The surfaces immersed in HBSS for (b) 1 h and (c) 1 week.

Figure 4. (Color online) (a–d) AFM images of air-annealed $TiO_2(110)$ surfaces with dimensions of 1000×1000 nm^2. Enlarged views of the terraces with dimensions of 200×200 nm^2 are shown in insets. (a) As-prepared surface. (b,c) Surfaces immersed in HBSS for (b) 1 h and (c) 1 week. (d) Surface immersed in Milli-Q water for 1 week.

Figure 5. (Color online) (a) Ball-and-stick models of the air-annealed TiO_2 surfaces. Light blue balls, red balls, and green large balls represent Ti atoms, O atoms, and hydrogen phosphate ions, respectively. (i) Possible active site for the calcium phosphate formation. The bridging O atom rows and the Ti atoms underneath are removed from the (1×1) structure. (ii) Arrangement of hydrogen phosphate ions on the active site. (iii) Arrangement of hydrogen phosphate ions on the (1×1) surface. (b) Ball-and-stick models of the $CaHPO_4$ sheet in the brushite crystal. Panels (i) and (ii) show views from the [010] and [001] directions, respectively. Yellow, green, red, and gray balls respectively represent Ca, P, O, and H atoms.

Figure 6. Survey scan XPS spectra of the air-annealed $TiO_2(110)$ surfaces that were further annealed in atmospheric-pressure O_2. (a) As-prepared surface. (b–c) Surfaces immersed in HBSS for (b) 1 h, (c) 1 week, and (d) 4 weeks.

Figure 7. Sets of O 1s, Ti 2p3/2, Ca 2p, C 1s, P 2p, and Mg 2p XPS spectra of the air-annealed TiO_2(110) surfaces with the subsequent annealing in O_2. (a) As-prepared surface. (b–c) Surfaces immersed in HBSS for (b) 1 h, (c) 1 week, and (d) 4 weeks.

Figure 8. (Color online) (a–d) AFM images of O_2-annealed TiO_2(110) surfaces with dimensions of 1000 × 1000 nm^2 with enlarged views of 200 × 200 nm^2. (a) As-prepared surface. (b–c) Surfaces immersed in HBSS for (b) 1 h, (c) 1 week, and (d) 4 weeks.

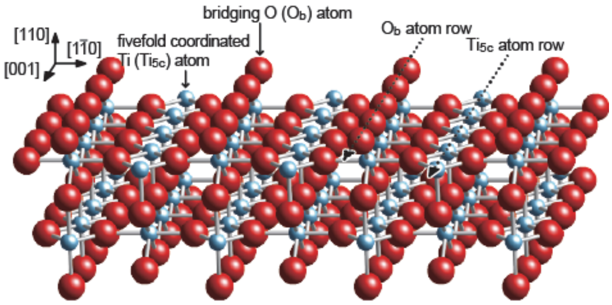

Fig. 1. (Color Online)

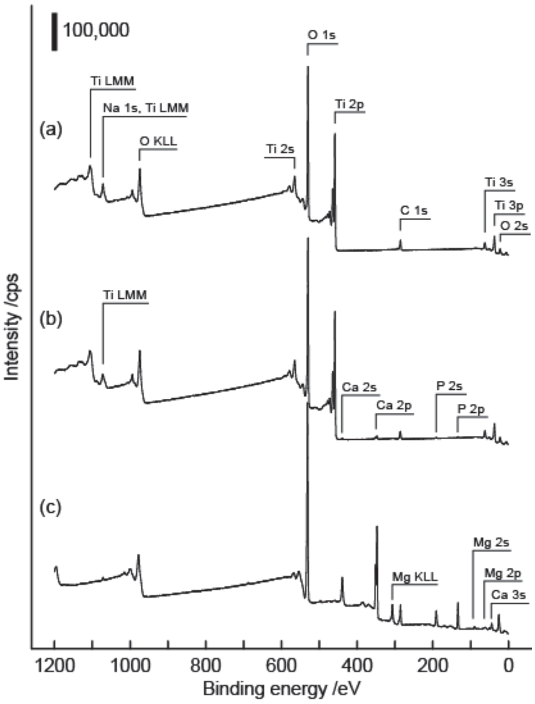

Fig. 2.   (Black and white)

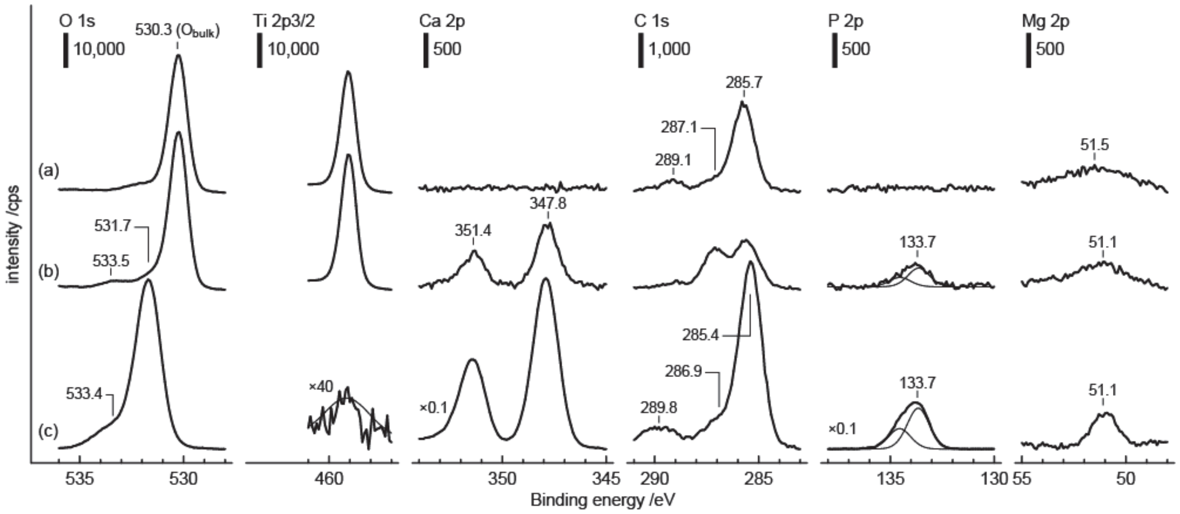

Fig. 3. (Black and white)

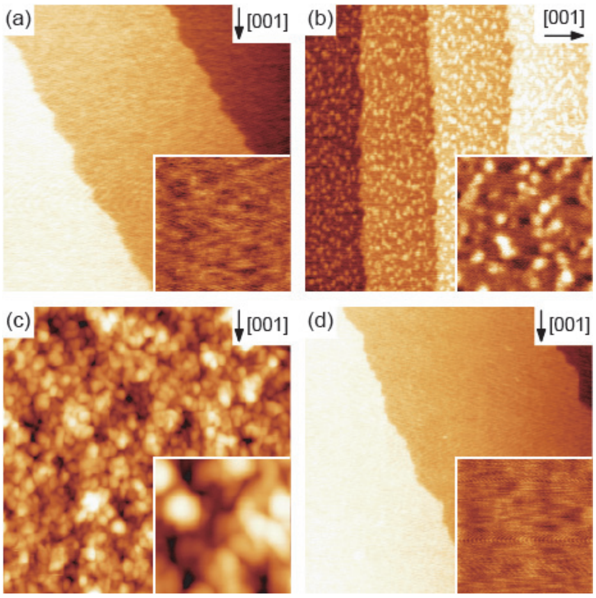

Fig. 4. (Color Online)

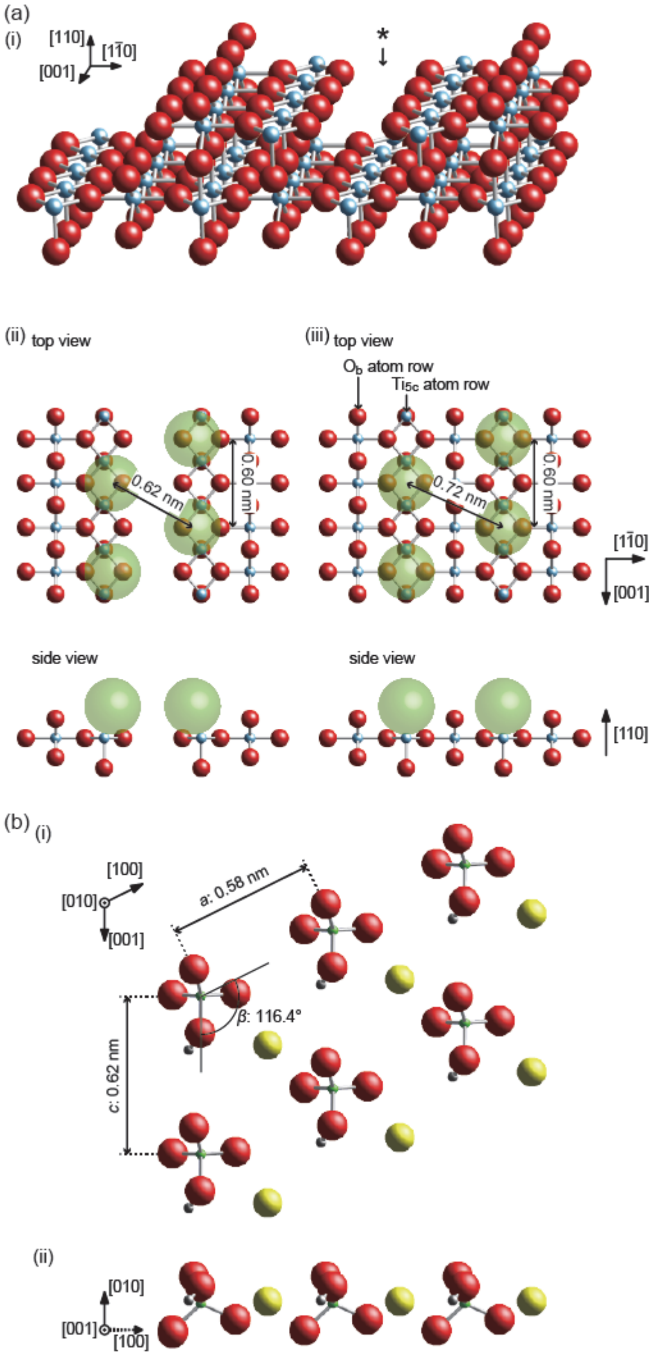

Fig. 5. (Color Online)

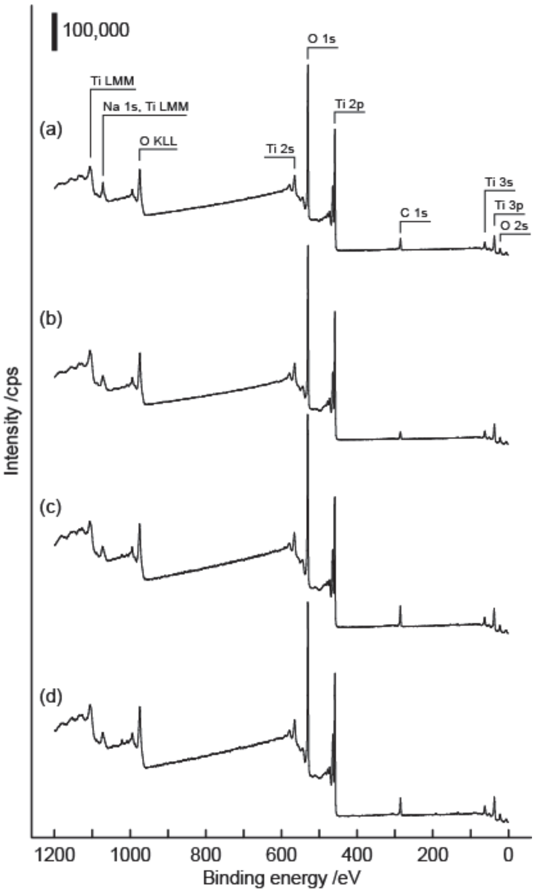

Fig. 6. (Black and white)

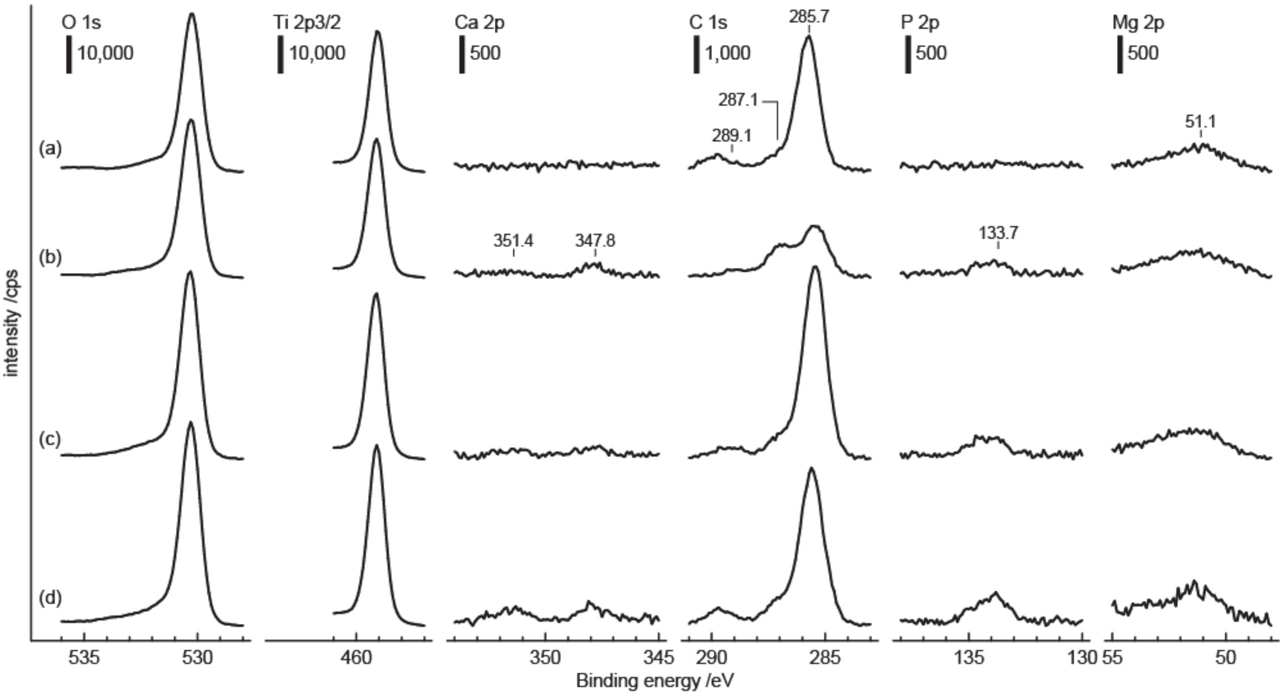

Fig. 7. (Black and white)

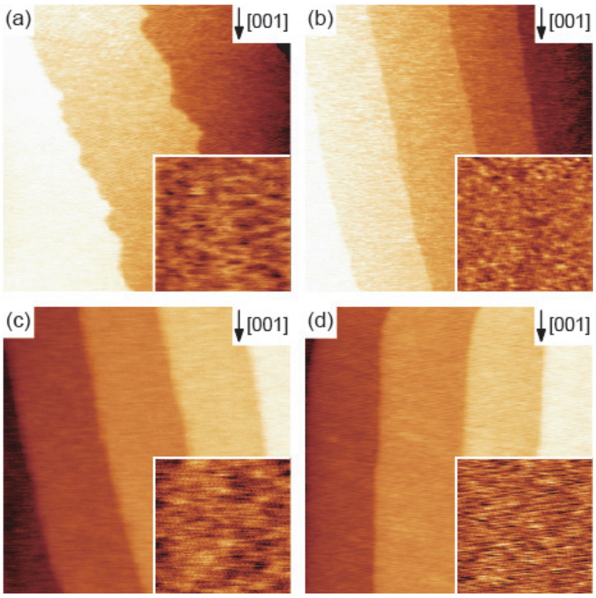

Fig. 8. (Color Online)